JOURNAL OF AIRCRAFT
Vol. 41, No. 6, November–December 2004

HELIPLAT: Design, Aerodynamic, Structural Analysis of Long-Endurance Solar-Powered Stratospheric Platform

Giulio Romeo,* Giacomo Frulla,† Enrico Cestino,‡ and Guido Corsino‡
Politecnico di Torino, 10129 Turin, Italy

This paper presents the design and manufacture of the first European Very Long-Endurance Stratospheric Unmanned Air Vehicle, HeliPlat® (HELIos PLATform).§ This vehicle is a monoplane with eight brushless motors, a twin-boom tail type and two rudders. A computer program has been developed to carry out the platform design. To minimize airframe weight, high modulus carbon fiber composite material has been used extensively. Airfoil coordinates and wing planform have been optimized in order to achieve the best possible aerodynamic efficiency by using integral panel/boundary-layer methods and also to obtain the minimum possible induced drag with respect to local Reynolds airfoil. To this effect, several wind-tunnel tests were carried out so as to compare the analytically predicted airfoil performances. After an initial configuration had been worked out, a scale technological demonstrator (wing span 24 m) was designed, manufactured, and tested under shear, bending, and torsion loads. Finite element analysis was also carried out in order to predict the static and dynamic behavior of both the full-size and scale model versions of the HeliPlat structure. The preliminary static test resulted in a high correspondence.

Nomenclature

b_w, b_{ht}, c_w, c_{ht}	=	wing (w) or horizontal tail (ht) span and chord
C_D, C_L	=	drag and lift coefficients
E	=	C_L/C_D, aerodynamic efficiency
E_1, E_2	=	lamina Young's modulus along fiber direction and normal fiber direction
e	=	Oswald's efficiency factor
F	=	fuel cells energy density
G_{12}	=	lamina in plane shear modulus
n	=	limit load factor
P_{req}	=	required power for horizontal flight
Re	=	Reynolds number
S_{ht}, S_w	=	horizontal tail and wing area
V	=	platform airspeed
W_{af}, W_{tot}	=	airframe and total platform weight
Z	=	altitude
α	=	incidence angle
η_{blade}	=	propeller efficiency
η_{fc}, η_{sc}	=	fuel-cell and solar-cell efficiency
η_{gears}, η_{inverter}, η_{motor}	=	reduction gear, inverter, and electric motor efficiency
η_{prop}	=	propulsion system efficiency
λ	=	aspect ratio
ν_{12}	=	lamina Poisson's ratio
ρ	=	air density
ρ_c	=	lamina density
σ_{1R}^t, σ_{1R}^c, ε_{1R}^t	=	lamina tension and compression failure stress and strain along fiber direction

Received 29 May 2003; revision received 26 September 2003; accepted for publication 27 September 2003.

*Full Professor of Airplane Design and Aerospace Structures, Department of Aerospace Engineering, Corso Duca degli Abruzzi 24; giulio.romeo@polito.it.

†Assistant Professor of Aerospace Structures Analysis, Department of Aerospace Engineering, Corso Duca degli Abruzzi 24.

‡Researcher of Airplane Design, Department of Aerospace Engineering, Corso Duca degli Abruzzi 24.

§® Trademark of Dept. of Aerospace Eng., Politecnico di Torino.

I. Introduction

NOWADAYS there is a growing request for Very Long Endurance Solar–Powered Autonomous Aircraft (VESPAA) flying at stratospheric altitudes of 17–25 km because they can act as artificial satellites—with the advantage of being much cheaper, closer to the ground, and being able to perform missions that offer greater flexibility. They could in fact be self-launched, easily recovered for maintenance whenever necessary and moved to cover different regions if desired. In addition, they allow a more detailed land vision because of their relative closeness to the Earth—at a cost far lower than the $ 200–300 million needed for a conventional satellite. The missions of such platforms could cover a wide range of applications: atmospherical pollution control and meteorological monitoring, real-time monitoring of seismic-risk areas, coastal surveillance, and telecommunications services such as cellular—telephone networks, video-surveillance, photogrammetry, hydrographic monitoring system, agriculture monitoring, and so on. From a flying altitude of 18 km, an area of about 300 km in diameter would be covered for communication transmission if the onboard antenna irradiation diagram is properly chosen. This would mean that just four to five platforms could cover the whole of Italy from North to South and seven to eight platforms could cover the entire south Mediterranean Sea from Spain to Turkey (Fig. 1), creating an electronic anticlandestine immigration barrier as well as a secure border control system.

The vehicle should climb to 17–20 km by taking advantage mainly of direct sun radiation and should thereafter maintain a level flight pattern. Any electrical energy not required for the propulsion and payload operations is pumped back into the fuel-cell energy storage system; during the night, the platform would maintain altitude thanks to its stored (solar) energy, and its geostationary position would be maintained by a level turning flight.

Several types of high-altitude stratospheric platforms (HASP) have been designed in the past.[1–5] At the end of 1994, NASA started the Environmental Research Aircraft and Sensor Technology (ERAST) program; one of the four drones is the solar platform Pathfinder, which exceeded 24 km of altitude in a 15-h flight. In the summer of 2001, the Helios solar-powered platform set a new world record of 29350 m. Although a flight of several days was planned for summer 2003, the program suffered a devastating setback when

Fig. 1 Pictorial view of HeliPlat service over Mediterranean Sea.

the Helios prototype was lost in June 2003 in a flight mishap during a shakedown mission.

Research into solar-powered platform started at our Technical University in 1995, thanks to financial support from the Italian Space Agency (ASI): the aim was to design a VESPAA and manufacture a scale-sized solar-powered prototype. Because of the limited financial support, only a small part of the research has been completed; nevertheless, a great deal of experience has been gained in this field.[6–13]

A great impulse to the design and manufacture of the VESPAA HeliPlat® has been obtained through the HeliNet program (network of stratospheric platforms for traffic monitoring, environmental surveillance and broadband services, coordinator being the Politecnico di Torino). Since January 2000, this has been financed by the European Commission within the Fifth Framework Program, with a view to developing the first European project in the field of stratospheric platforms.

II. Platform Design

The main advantages of the very long-endurance high-altitude solar-powered platform with respect to combustion engine configurations can be summed up as follows: 1) reduction in cost per flight hour by greatly increasing endurance flight hours; 2) reduction in maintenance and spares costs (though the acquisition cost might be higher); 3) reduction in total costs caused by larger area coverage per aircraft, thereby requiring fewer aircraft per area; and 4) improved operational safety because flight remains above aviation traffic and above adverse weather conditions and also has fewer climb and descend events, resulting in limited interference with aviation traffic.

The only real disadvantages of solar-powered platforms are the payload weight (less than 1500 N) and the power available for the payload (1000–1200 W).

It cannot be denied, however, that certain hurdles need to be surmounted before VESPAA can become fully operational and cost effective. First of all, because today's solar cells convert such a small percentage of the sun's energy into useful work the platform has to be of considerable dimensions. Its sun-powered level flight can only be obtained through a suitable design coupled with an accurate and ultrahigh standard integration of each technological item involved: structural weight optimization, aerodynamics, solar cells, fuels cells, propulsion efficiency, and electronic devices.

To date, it has been the low effectiveness of solar cells that has adversely affected the development rate of solar-powered platforms. High efficiency (15–16%), thick (200–300 μ), single-crystal silicon cells are now available at a low price (about 800 \$/m^2); also, higher efficiency (up to 22%), very thin (50–70 μ), single-crystal silicon cells are now available, although at a far higher price (about 30,000 \$/m^2).

An efficiency of 96% can be obtained through the careful design of the rare-Earth-magnet brushless electric motor. To this end, a research project is being carried out in the Department of Industrial Electrical Engineering of Turin Polytechnic University concerning a novel axial flux permanent magnet brushless electric motor with a composite materials structure.[14] The prototype has already been manufactured and is being tested so as to compare the analytical data. In parallel, with the assistance of simulation software an analysis is being conducted of the structure and architecture of the power conditioning system (dc/dc converter) for the interface between the aircraft's fuel-cell and solar-cell supply sources and the propulsion system (motor + inverter).

Fuel-cell efficiency presents another hurdle to surmount. In general such systems are based on the electrolysis of water, the storage of hydrogen and oxygen, and the following recombination to water in a fuel cell during power production. Because present-day efficiency is about 55–60%, the ambitious goal of an energy density of 500–600 Wh/kg has yet to be reached in designing the energy storage system (based on dedicated electrolyses and fuel cells of the solid polymer type).

The choice of a flying altitude between 17 and 20 km (Refs. 7 and 12) for the solar platform HeliPlat takes into account two factors: first, the solar radiation available in Southern Europe from 45–37° latitude North (Milan, Belgrade, Toulouse, Rome, Madrid, Athens, Istanbul, Sicily, Malta, etc.); and second, the wind profile as a function of the altitude. At the altitude chosen, in fact, the jetstream speed has a relatively low value.

Even though the average wind-speed value in Southern Europe in winter at 18 km of altitude is less than 14 m/s, consideration of the standard deviation gives an 86% probability of occurrence for a maximum speed of 24 m/s. The speed rises to 29 m/s at a 95th percentile and to 36 m/s at a 99th percentile.[12] Different seasons, however, evidence lower values of the wind speed. Our investigation of the occurrence of high jetstreams recorded from 1963–1997 shows that in January 60% of the events were in a speed range lower than 15 m/s; a speed higher than 35 m/s was recorded only 60 times in over 2000 events in 34 years. This leads to the conclusion that the aircraft's propulsion power should be able to contrast a jetstream of 35 m/s, although such a necessity should occur only in a very few instances.

For the HeliPlat solar platform presented in this paper, the design procedure followed in the analysis[7,10,12] is based on the energy balance equilibrium between the available solar power and the required power, the former being dependent on the solar-cell area installed on the wing and stabilizer, the latter depending on the velocity and total drag of the platform. In particular, the endurance parameter has to be fulfilled in order to minimize the power required for horizontal flight. This means minimizing the parameter $C_D/C_L^{3/2}$; because of the lower structural load, we also chose to reduce the drag coefficient C_D instead of simply increasing the lift coefficient C_L. The total drag, coefficient is obtained from the sum of the wing-and-tail profile drag, wing-and-tail-induced drag and parasite drag (fuselage, booms, interaction with wing and tails). Reynolds numbers of less than 7×10^5 should be considered. The induced drag in the wing or tail is computed as a function of the aspect ratio λ and Oswald's efficiency factor e (to take into account the nonellipticity of the lift distribution):

$$C_{\mathrm{Di}} = C_L^2 \big/ e\pi\lambda \tag{1}$$

The power per unit wing area P_{req}/S_w needed to maintain horizontal flight is given by

$$P_{\mathrm{req}}/S_w = (2/\rho)^{0.5}(W_{\mathrm{tot}}/S_w)^{\frac{3}{2}}\left(C_D \Big/ C_L^{\frac{3}{2}}\right)/\eta_{\mathrm{prop}} \tag{2}$$

where the propulsion efficiency η_{prop} is given by $\eta_{\mathrm{prop}} = \eta_{\mathrm{blade}}\eta_{\mathrm{gears}}\eta_{\mathrm{motor}}\eta_{\mathrm{inverter}}$.

The total power required is obtained by adding the power required by the payload and avionics.

To be remembered, not only must the available power produced by the solar cells give the power for daylight equilibrium, but it must also regenerate the fuel cells for night flight.

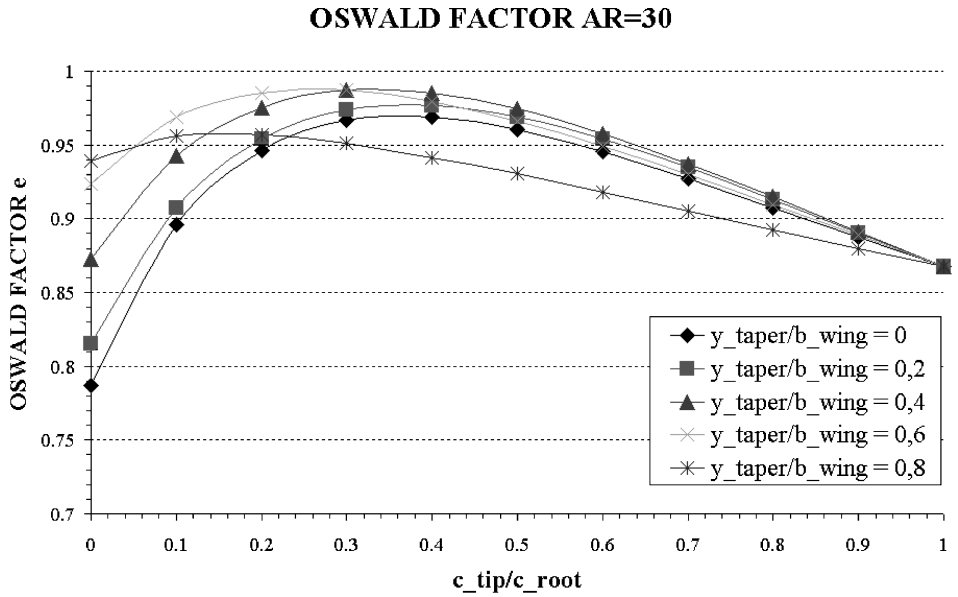

Fig. 2 Oswald's efficiency factor as a function of the taper ratio.

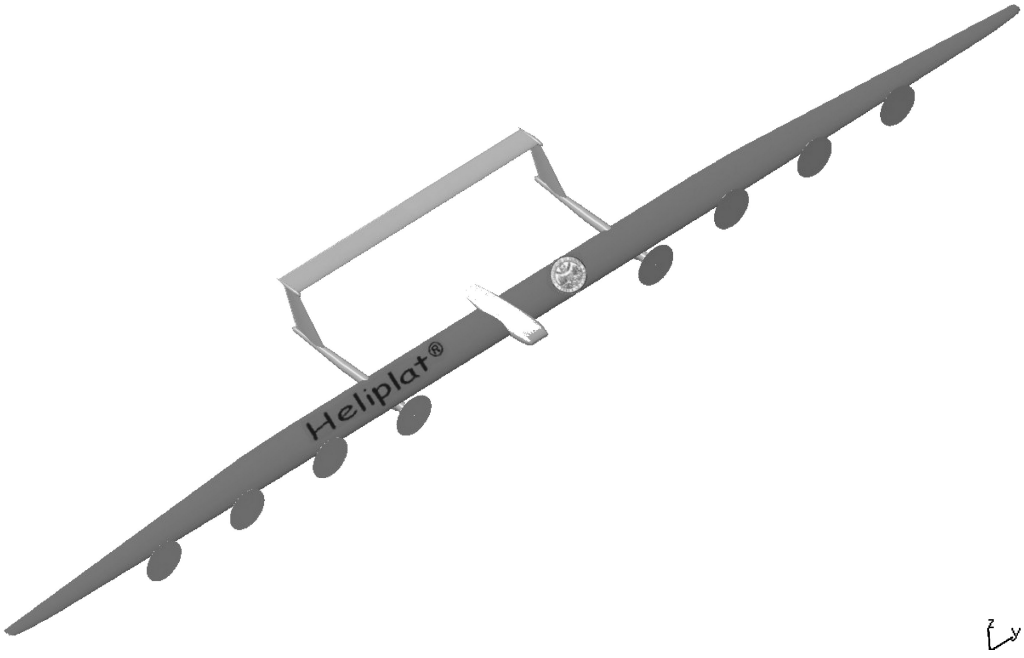

Fig. 3 HeliPlat optimized configuration.

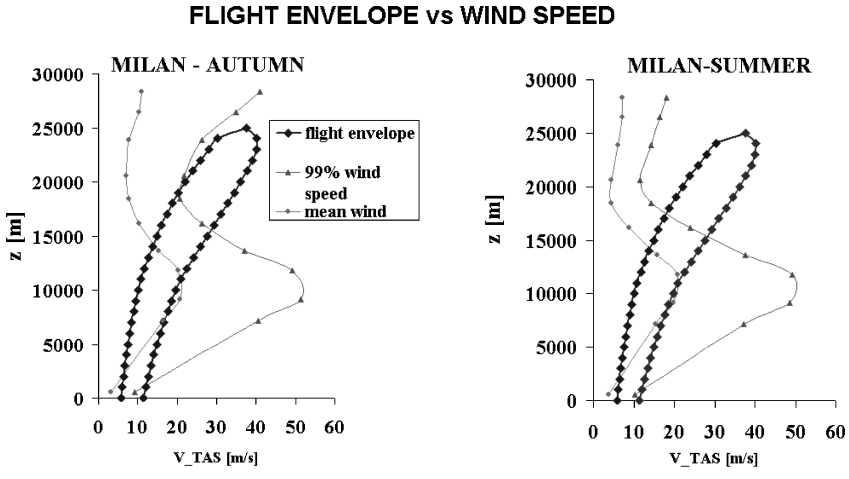

Fig. 4 HeliPlat flight envelope and wind speed.

To complete the power equilibrium, an airframe mass estimation of the platform is necessary. The following expression has been derived for the airframe weight:

$$W_{\text{airframe}} = 8.75 n^{0.311} \lambda^{0.4665} S_w^{0.7775} \tag{3}$$

The total platform weight per wing area is determined by adding the weight of propulsion, solar cells, avionics, and payload to the airframe weight. The solution of all of the preceding equations gives the total platform area, as a function of the aspect ratio and weight, producing a balance between required and available power.

A preliminary study of the main parameters influencing the platform dimensions has already been carried out.[10,12] A significant reduction in platform size (Wing area and span—thereby expanding mission range, altitude, or latitude sites) can be obtained by increasing the specific energy of the fuel cells to 600 Wh/kg and their efficiency to 70%; note that solar-cell efficiency and weight can also play an important role in flight performance. The present

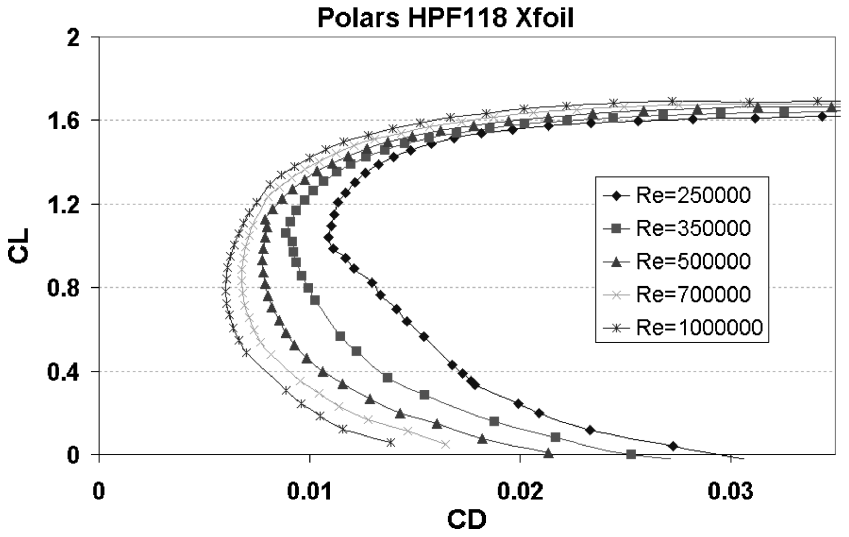

a)

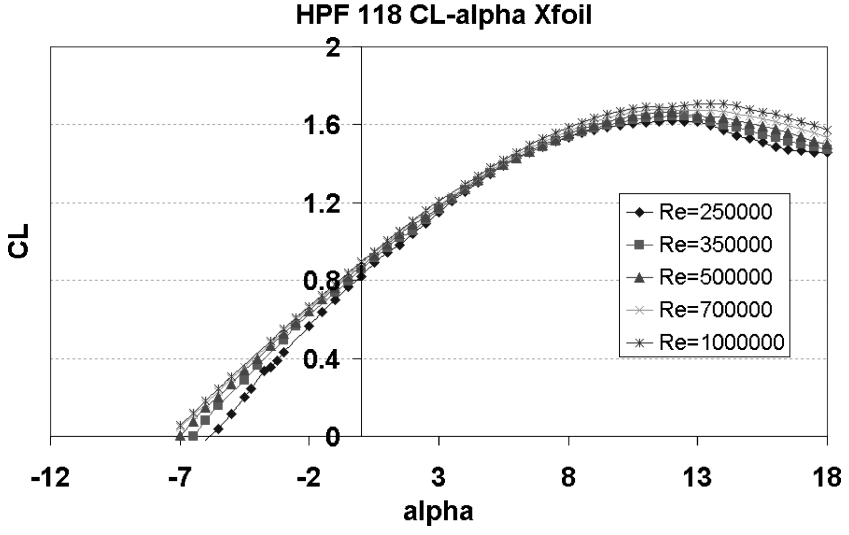

b)

Fig. 5 Aerodynamic performances of the HPF-118 airfoil.

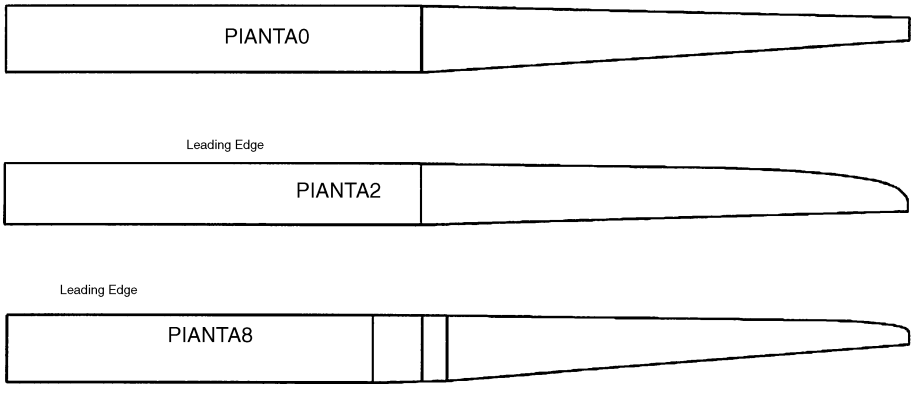

Fig. 6 Various planform surface shapes investigated.

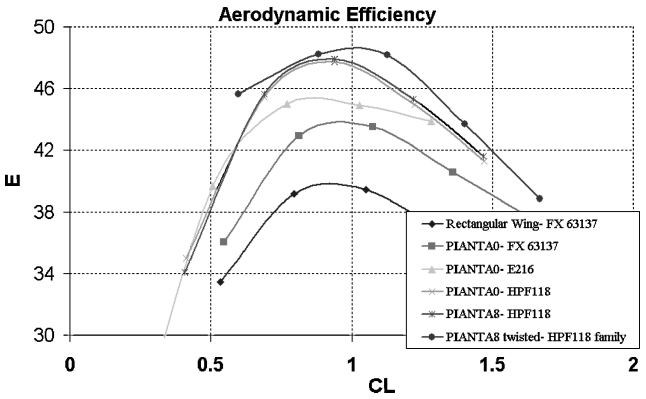

Fig. 7 Aerodynamic efficiency as a function of wing surface shape and airfoil.

Fig. 8 Wind-tunnel facility at IAG University of Stuttgart.

day solar-cell efficiency of 21% would be acceptable if it could be obtained at a lower production cost because at present rates the cost of these cells (about 30,000 $/m^2) drastically increases the acquisition cost of this type of platform ($6 million for the solar cells alone out of an estimated total platform cost of $10 million).

Another factor requiring attention is wing-induced drag, obviously to be reduced to the minimum achievable. Here is where wing planform configuration comes into play. Following on the extension of Prandtl's lifting-line theory to curved wings in a computer program, whose aim is to show the effect of curved geometry on aerodynamic efficiency,[15] we have performed a wide numerical analysis investigating Oswald's factor variations with regard to different wing parameters: aspect ratio λ, taper ratio (taper $= c_{\text{tip}}/c_{\text{root}}$), starting point of the taper chord, nondimensionalized with respect to the half-span (y_tap). This analysis refers to a nontwisted wing.

The variations in Oswald's efficiency factor have been computed, as a function of the aspect ratio and for different values of the taper ratio, for a rectangular/trapezoidal wing with a taper starting at 40% of the half span (y_tap $= 0.4$). Efficiency always decreases with regard to the aspect ratio for all of the configurations considered, the worst configuration being the rectangular/triangular wing (taper $= 0$), with the all-rectangular wing (taper $= 1$) also resulting in a low efficiency value (around 0.85). The maximum efficiency value (around 0.98) holds for a taper ratio of 0.4, with a slightly lower value for a taper ratio of 0.2. Oswald's efficiency factor (OSW) plotted in Fig. 2 as a function of the taper ratio for a fixed value of the aspect ratio ($\lambda = 30$) and for the different abscise values at which tapering starts (y_tap). It can be seen here that maximum efficiency is reached for y_tap values between 0.4 and 0.6 in a taper range of between 0.2 and 0.4. Because it is well known that a rectangular wing is not the best configuration for reducing induced aerodynamic drag (to which a low value of Oswald's factor corresponds), the adopted rectangular/trapezoidal configuration (with specific values of the shape parameters) has turned out to be an optimum solution giving a performance very similar to an elliptical configuration.

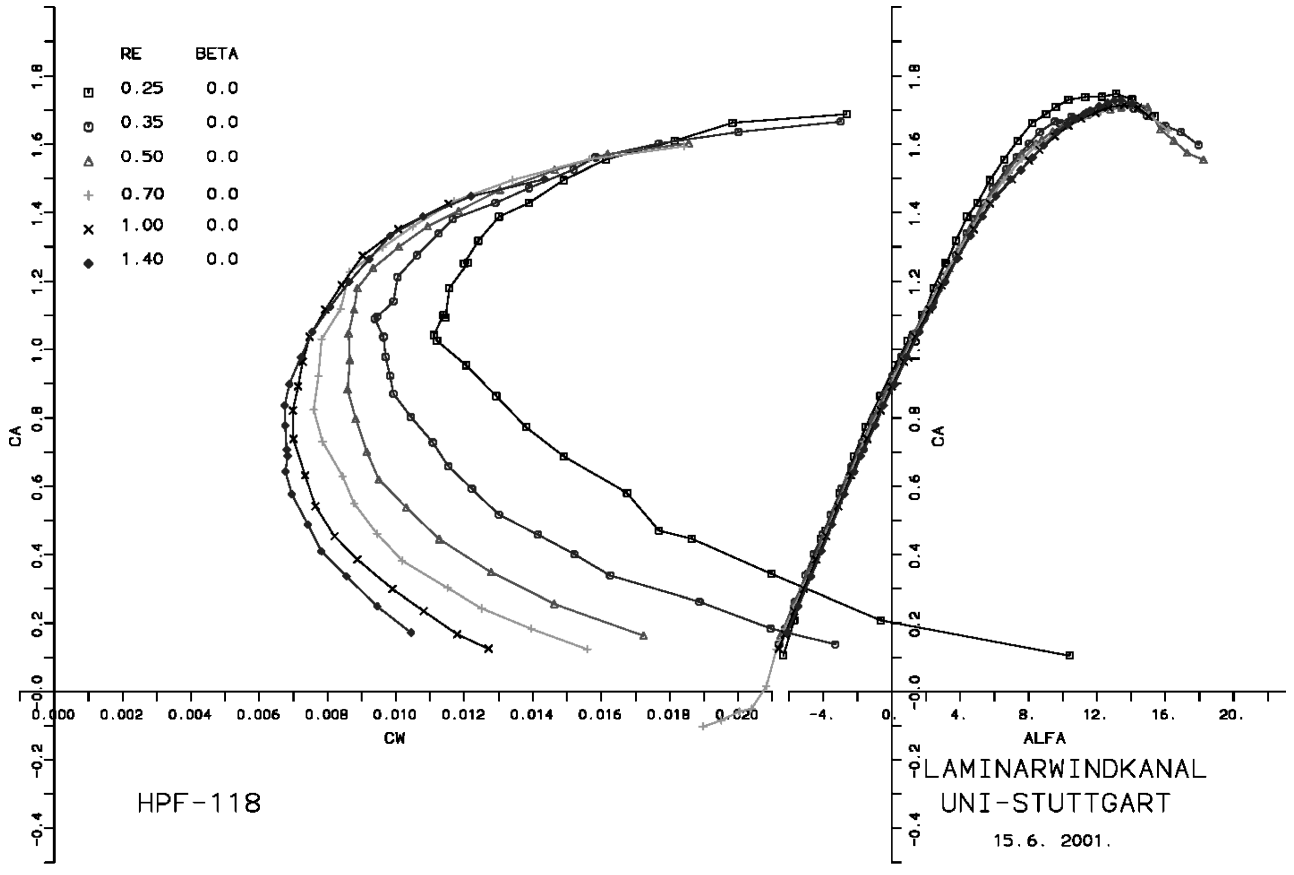

Fig. 9 Experimental results of the HPF-118 airfoil.

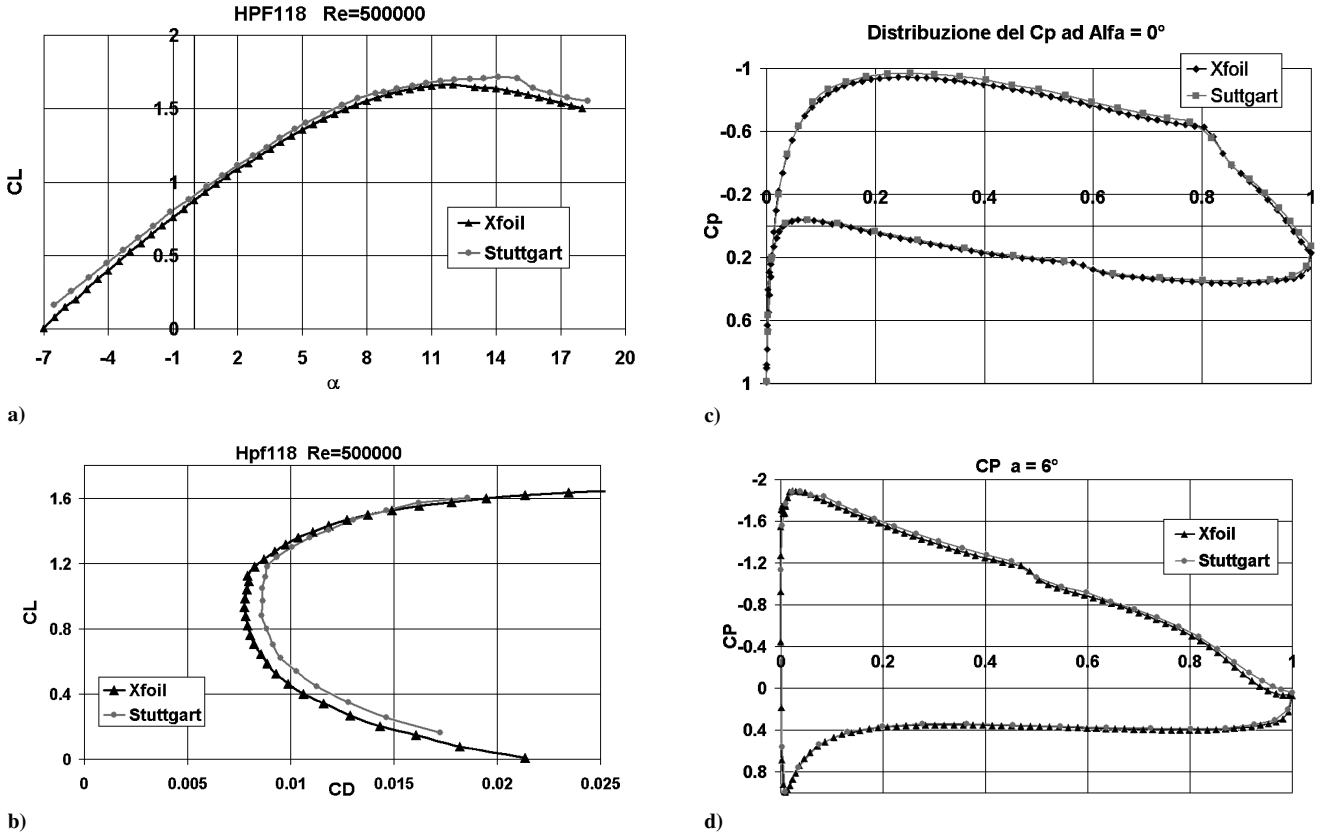

Fig. 10 Comparison between experimental and analytical results of the HPF-118 airfoil.

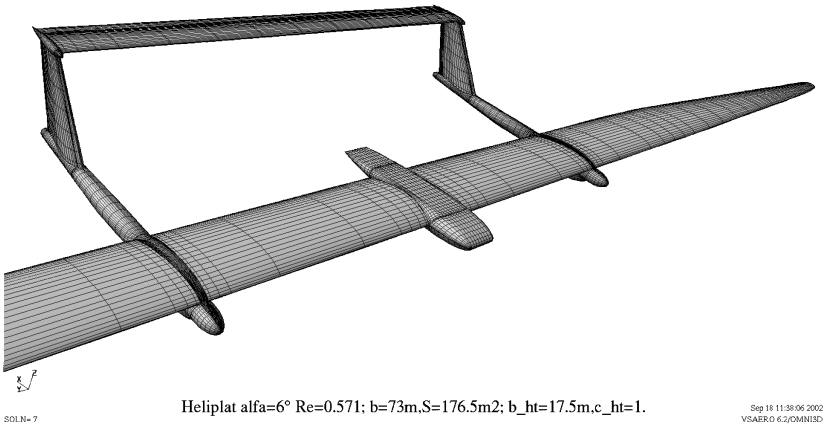

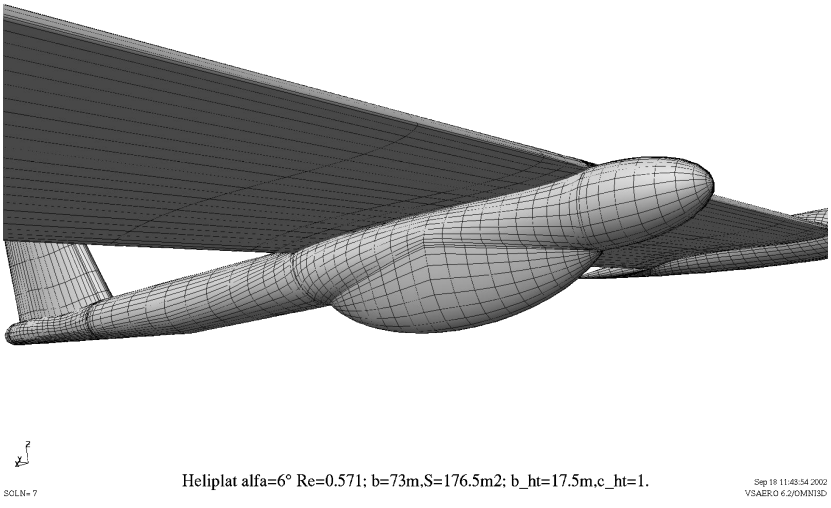

Fig. 11 Platform grid generation using VSAERO.

III. HELIPLAT Configuration

As a result of the parametric study, a specific configuration of HeliPlat (Fig. 3) was worked out: a monoplane with eight brushless motors, a twin-boom tail type with a long horizontal stabilizer, and two rudders.

The main characteristics for a nine-month flight (starting 1 February), at 38°N latitude and design altitude of 17 km, carrying a payload of 981 N, are $W_{\text{tot}} = 8000$ N; $P_{\text{req}} = 6500$ W; $P_{\text{payload}} = 1000$ W; $n_{\max}$: 3.1; $V_c = 71$ km/h (TAS); $\eta_{\text{sc}} = 0.2$; $\eta_{\text{fc}} = 0.6$; $\eta_{\text{prop}} = 0.81$, $S_w = 176\,\text{m}^2$; $b_w = 73$ m; $c_{w\text{root}} = 2.97$ m; $\lambda_w = 31$; taper ratio $= 0.32$; $S_{\text{ht}} = 28\ \text{m}^2$; $b_{\text{ht}} = 17.5$ m; length $= 11$ m; height $= 4.2$ m; $E = 36$; and $C_L^{3/2}/C_D = 45$.

A classical wing-tail configuration was chosen over the all-wing Helios project because a simpler flight-control system would be required; a rectangular-trapezoidal wing planform was preferred to the all-rectangular wing in order to reduce wing-induced drag by 13%.

The choice of eight motors represents a good compromise between redundancy (see next paragraph) and mass; the surplus power required for the system was established as 5000 W for 2 h in order to continue aircraft functions during periods of extremely high wind-speed jets (35 m/s). The boom tail configuration was chosen to permit the installation of the oxygen and hydrogen tanks. The airframe (weight 3555 N) is about 44% of the total weight, that of the solar cells (1250 N) 16%, the fuel cells (1550 N) 19%, the propulsive system (510 N) 6%. Restricting to nine months per year the amount of time the platform is required to fly (thus avoiding the darkest period of the year) resulted in several advantages: a significant reduction in platform size, a limitation of wing span to only 73 m, and the ability to manufacture the platform with present solar-cell technologies. As solar- and fuel-cell efficiencies increase in the future, it should be possible to extend flight life to the entire year.

The flight envelope of the HeliPlat Platform is presented in Fig. 4 as a function of the flight altitude and horizontal speed for autumn and summer flights, respectively. The horizontal wind speed (as recorded over 34 years of twice-daily measurements at established standard altitudes) is plotted in the same figure. Both the average horizontal speed value and the 99% statistical occurrence value are plotted; in both cases, the platform configuration would be able to contrast the maximum wind speed recorded during this period.

IV. Preliminary Reliability

From the preliminary reliability design performed for the definition of HeliPlat's propulsion configuration,[16] a multiple-unit propulsion system was found to be necessary for efficient propeller design and for the required level of system reliability (long endurance, redundancy). The usual simplifying assumptions introduced into the calculations can be seen in Ref. 17. The design rate of failure presented was obtained by means of considerations regarding fleet reliability (standby platforms), assuming a mission reliability (probability of covering a specific service) of 1E-6 and a fleet of six flying platforms plus up to four standby platforms. A reference failure rate of less than 5E-6 has been calculated by means of a parametric analysis that verifies the requirement when four platforms are in standby (assumed duration). In the definition of the failure rate of the platform, only the effect of the propulsion units has been considered. A failure rate of 2E-5 for each propulsion unit is introduced into the total of eight units, a minimum of two working units for each half-wing, obtaining a failure rate of less than the reference value for each chosen duration.

In selecting the configuration of the propulsion unit,[16] two unit configurations were studied: a motor propeller series system (case A) and a two-motor-one-propeller system (case B). These two cases were introduced into the half-wing: four units of case A (at least two propellers operating); two units of case B (two propellers operating but four motors connected); and four units of case B (at least two half-wing propellers operating but eight motors connected). Single-unit A proves less reliable than single-unit B; however, the weight of B is double that of A. If the units are inserted in a half-wing with the same number of propellers, the system composed of A units seems more feasible from the weight point of view. If B units are used, a reduced number of propellers is required so as to keep the weight down to the same level. The propeller therefore becomes the most critical component: the loss of one propeller causes the loss of its two connected motors. Redundancy can mitigate this, but the increase in weight is obviously undesirable. An increment in the number of A units is referable and is the solution adopted for the HeliPlat design.

V. Aerodynamic Analysis

The aerodynamic analysis of the HeliPlat configuration has been carried out. Because the platform must fly at very high altitudes (17–20 km) and low speeds, a low Reynolds number (4×10^5–8×10^5) is expected. A wing profile with a high lift coefficient and low drag coefficient would be necessary to reduce wing and horizontal tail drag; unfortunately, though—because of low Reynolds numbers—laminar separation bubbles represent a serious problem because boundary layers become large and increase the boundary displacement thickness, which can have an appreciable effect on the inviscid pressure distribution; they substantially increase drag and decrease performance. Theoretical methods are able to predict fairly accurately the lift coefficient as a function of the incidence angle, maximum lift coefficients and stalling behavior, profile polars, etc.[18] However, because some simplified hypothesis are introduced into the analysis (regarding for example turbulence level, boundary-layer transition, and bubble separation prediction), wind-tunnel tests then become necessary to obtain an accurate behavior of the profile.

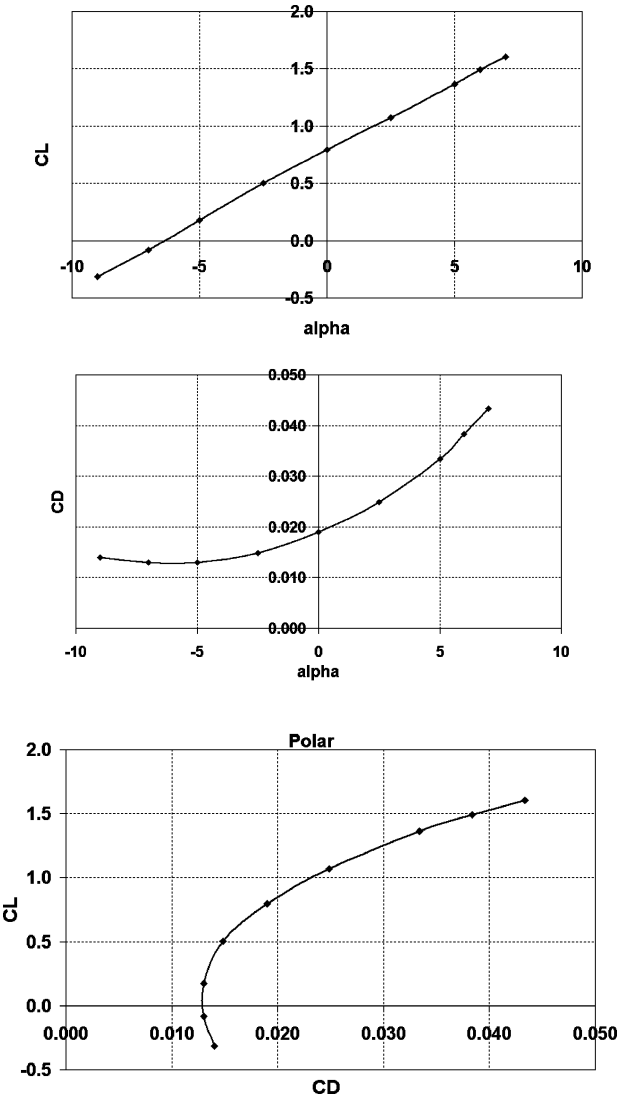

Fig. 12 HeliPlat aerodynamic performances.

The production of a highly accurate wind-tunnel model, including several static-pressure tabs for pressure distribution measurements, is necessary for wind-tunnel tests in a low-speed-low-turbulence wind-tunnel. Calculation of the pressure distribution over the entire wing can be affected (providing a potential flow pressure distribution exists) by using the panel method program.[19] The platform and airfoil coordinates at the root and tip and positions of the taper ratio change have to be specified, as well as the angles of attack. A viscous flow pressure distribution is also possible through the computer program VSAERO. At present the aerodynamic design of the platform is being completed using the XFOIL code to obtain profile performances, in association with the VSAERO code to obtain performances for the entire wing and aircraft. XFOIL uses the Euler equation to solve the inviscid flowfield coupled with a two-equation dissipation integral method to solve for the viscous boundary layer.[18]

A. Airfoil Performance

A wide number of different standard profiles (Eppler 216, Ah-95-160, Ah-94-145, dae-21, Fx 63-137, Fx 73-xxx, MH-32, etc.) were evaluated for Reynolds numbers between 4×10^5 and 8×10^5 to compare the efficiency and endurance parameter of the several profiles available in literature.[20,21] An iterative procedure was followed until the final optimized aerodynamic solution was obtained.

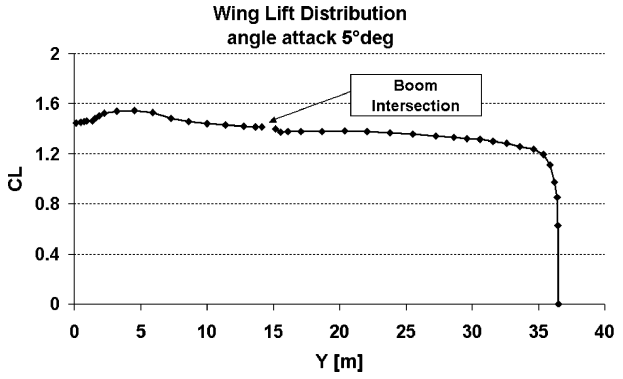

Fig. 13 Local lift coefficient along the wing span at 5-deg angles of attack.

Starting from a preliminary design of the HeliPlat platform, the performances were updated as the wing airfoils were changed.

In the first step (as is the case in many reports[2–4]), very high lift profiles were considered to be the most suitable for our project in order to increase the parameter $C_L^{3/2}/C_D$. After many iterations, however, it became very clear that working with very high lift coefficients was greatly increasing the induced drag of the lifting surfaces, thus reducing any benefit to the endurance parameter. In fact, the design of long-endurance solar-powered platforms requires a high value of wing surface to support the solar cells and recharge the fuel cells. This results in a low flight speed, reducing the correspondent Reynolds number and consequently increasing the profile drag. The local wing lift coefficient C_L is between 1.1 and 1.4, with Reynolds numbers of about 5×10^5–6×10^5. Using the VSAERO software,[19] the aerodynamic performances of several different wing profiles were also obtained. From this investigation, the E-216 airfoil emerges with a high efficiency level because of a better compromise between the profile drag and the wing-induced drag and an endurance parameter of 52; however, its low profile thickness (10.43%) would require the introduction of more material in the wing spar and so result in a heavier structure.

Starting from these preliminary results, the XFOIL interactive program was used to develop a new profile aimed at higher platform performance. This resulted in a high C_L and low C_D profile with different characteristics from the E-216 found in the literature. The aerodynamic performances of the new airfoil (HPF-118, thickness 11.8%) are plotted in Fig. 5 for various Reynolds numbers in the effective working range. Also plotted are the C_L-C_D curve and the C_L-α curves for several Reynolds numbers (Figs. 5a and 5b). It can be seen that the low C_D part of the profile polar is centered around the normal C_L flight of the aircraft, obtaining a low moment coefficient (desirable in aircraft equilibrium and stability control). A high efficiency of 140 was reached for a Reynolds number of 6×10^5 with a C_L of 1.2; a $C_L^{3/2}/C_D$ parameter of 160 was also obtained at the same values.

B. Wing Performance

Using the VSAERO software, an analysis was carried out to obtain the aerodynamic performance of the HeliPlat wing at the flight Reynolds numbers (3×10^5–7×10^5), with various wing aspect ratios and wing planforms. The aerodynamic efficiency of wings with constant planform areas but very different aspect ratios has been

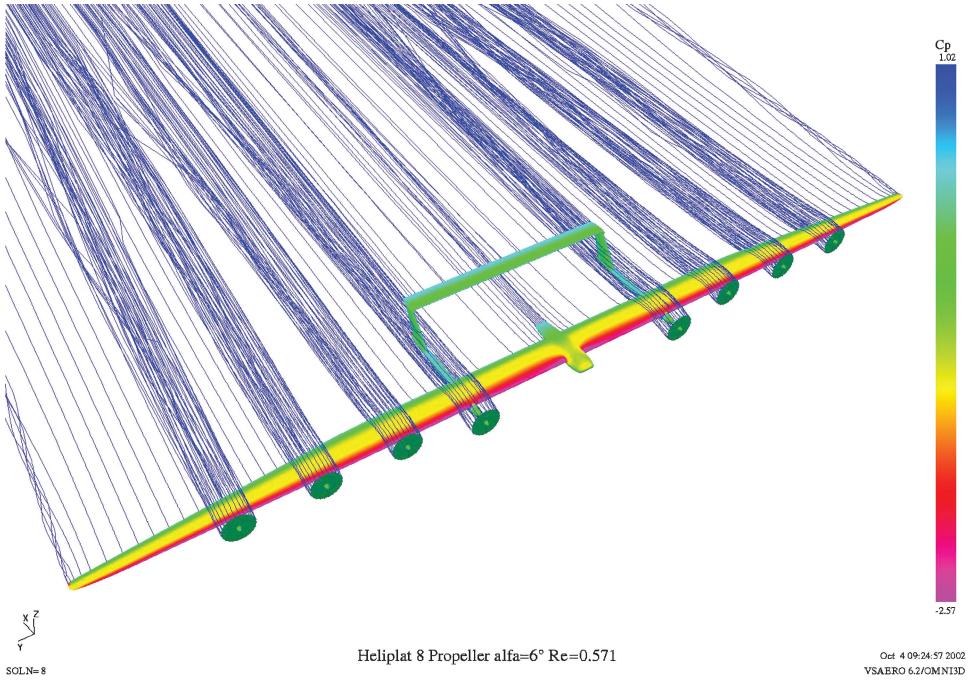

Fig. 14 Propeller wakes and upper surface pressure distribution of HeliPlat at 6-deg angles of attack.

studied, with the result that an increase in the aspect ratio gave a better performance; moreover, both the chord length and the local Reynolds number decreased. It is interesting to observe that an aspect ratio decrease resulted in a performance-loss percentage higher than the loss caused by an equivalent aspect ratio increase. This is true because increasing the aspect ratio of a constant wing surface means decreasing the chord length; however, increasing the ratio too greatly causes the low Reynolds profile drag to cancel the benefits, thereby giving lower performance. Several different wing planforms were taken into consideration, and two of them have been plotted in Fig. 6. Each wing has a constant span and an equal surface, that is, the same aspect ratio and equal foil along the span, with no twists. In attempting to minimize induced drag, it was found that some wing planforms increase friction drag more than they reduce induced drag (for example, PIANTA2 in Fig. 6). The minimum drag optimum configuration was found with PIANTA8. At this point it was decided to perform an optimization process that involved the twisted airfoil and curvature of the HPF118 foil along the wing span, aimed at obtaining the optimum work point of the airfoil. The stability stall behavior of the wing at high angles of attack was investigated in order to achieve a later stall of the wing tip with respect to the wing center. The resulting aerodynamic efficiencies of several HeliPlat wing planforms are plotted in Fig. 7. Each wing polar was obtained at the same wing load and at altitude z. The HeliPlat wing's highest efficiency value came out at 49.

VI. Wind-Tunnel Experimental Results of the Wing Profile

Several experimental tests have been carried out on the HPF 118 profile to verify the analytical results of the XFOIL software.

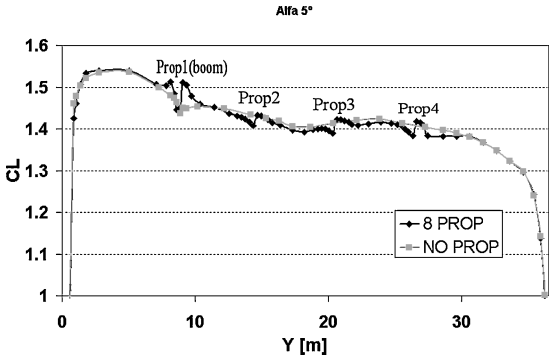

Fig. 15 Propeller effects on local lift coefficient along the wing span at 5-deg angles of attack.

A. Experimental Setup

The experimental tests were carried out by the Institut fur Aerodynamik und Gasdynamik—Universitat Stuttgart (IAG-US) in their Laminar Wind Tunnel (Fig. 8), an Eiffel design open return tunnel,[20,21] whose rectangular test section measures 0.73×2.73 m and is 3.15 m long. The two-dimensional airfoil models are mounted along the short distance of the test section and are fitted between two rotating plates in the tunnel walls. No air can flow by any leaks in the test section thanks to a subpressure chamber that surrounds the test section itself. The test-section turbulence level was measured with a hot-wire anemometer, in the range 0.012–0.049%, for the different Reynolds and velocity conditions. The airfoil model, built at the IAG-US workshop, has two wooden end ribs and three wooden stiffeners to increase its rigidity. Roughness heights of this model are in the order of 1-μm rms, measured with a high-precision surface measuring instrument.

The pneumatic system is connected to the scanivalve by mean of flexible PVC tubes. The lift is determined via integration of the pressure distributions along the two opposite tunnel walls. The equally spaced bores are connected via identical tubes to a common reservoir, which yields the average pressures along the opposite tunnel walls, and so the difference between the two average pressures is proportional to the lift. The drag is determined via integration of the total head loss in the wake by a rake of equally-spaced identical pressure tubes connected to a common reservoir, the pitching moment via the mechanical torsion around the quarter-chord pivot point. The data acquisition is controlled by a PC and carefully calibrated before each set of measurements. The aerodynamic coefficients determined are inclusive of standard tunnel corrections (0.9965 for C_L and 0.999 for C_D; pressure and moment coefficients have not been corrected).

B. Experimental Results and Comparison with Numerical Data

With the aid of the computational-fluid-dynamics (CFD) Xfoil software, a wide number of different situations have been evaluated for Reynolds numbers between 2.5×10^5 and 1.4×10^6 so as to analyze the effects of turbulence level, boundary-layer transition, and bubble-separation prediction. The calculated natural transition data were obtained by introducing a turbulence level correspondent to the clean wind-tunnel condition. The experimental results reported in Fig. 9 were also obtained at Reynolds numbers between 2.5×10^5 and 1.4×10^6.

A comparison with the analytical results is shown in Fig. 10. The C_L-α curve (Fig. 10a) and C_L-C_D curve (Fig. 10b) with natural transition are plotted for $Re = 5 \times 10^5$, the pressure coefficient behavior for the same Reynolds number is also plotted for angles of attack of 0 and 6 deg in Figs. 10c and 10d, respectively. At

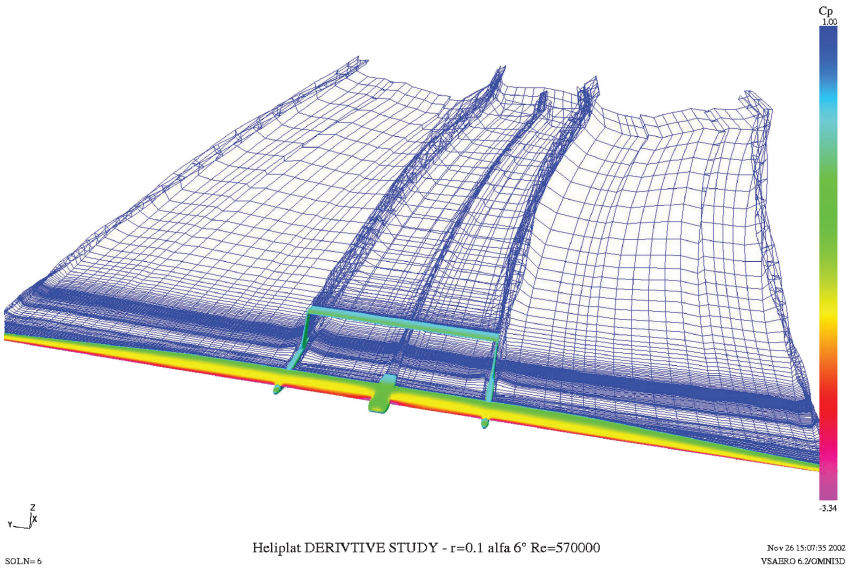

Fig. 16 Yaw angular speed effects on the wake shape.

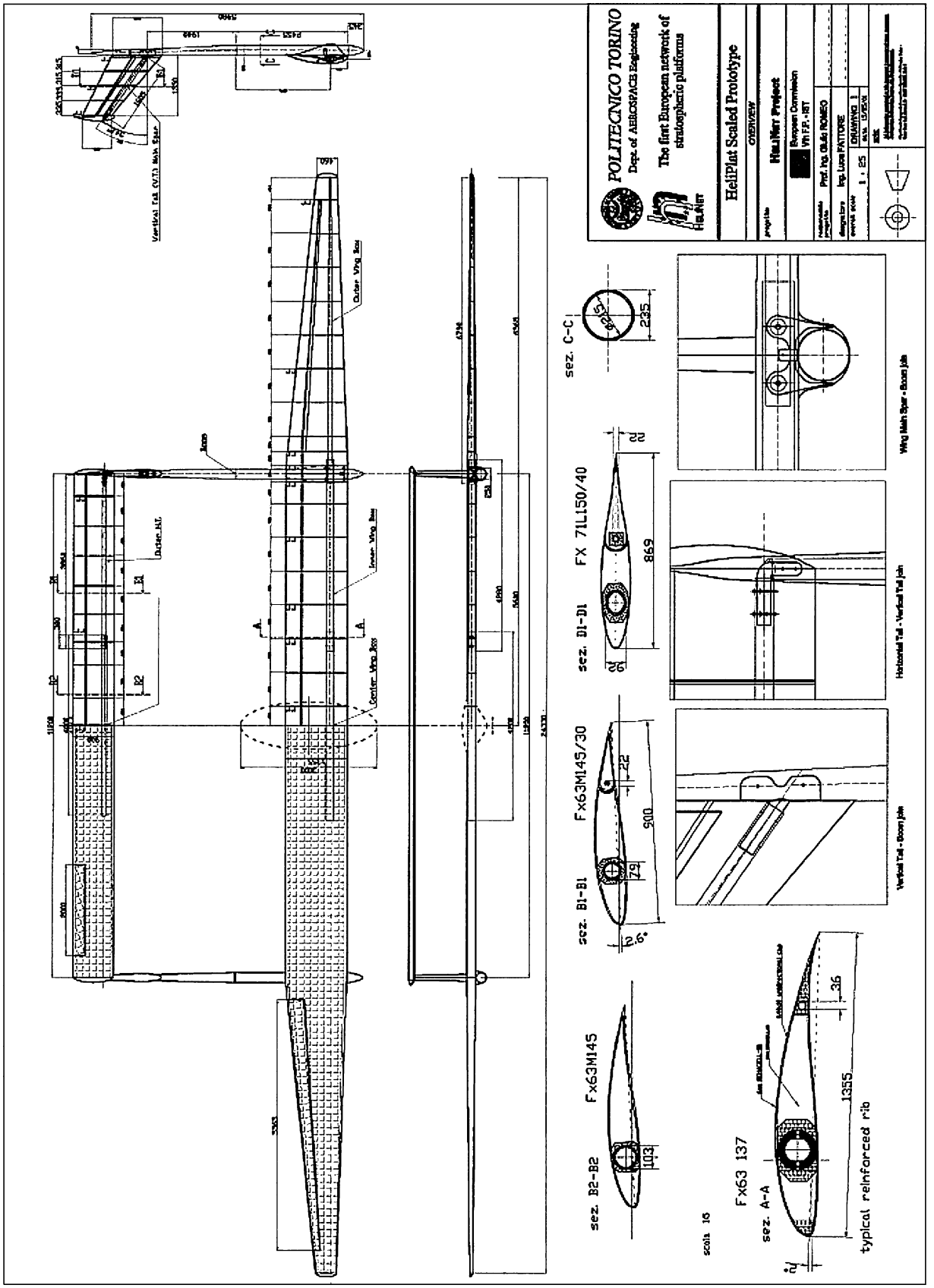

Fig. 17 HeliPlat scaled-size structural configuration; details of wing, horizontal tail, and boom sections.

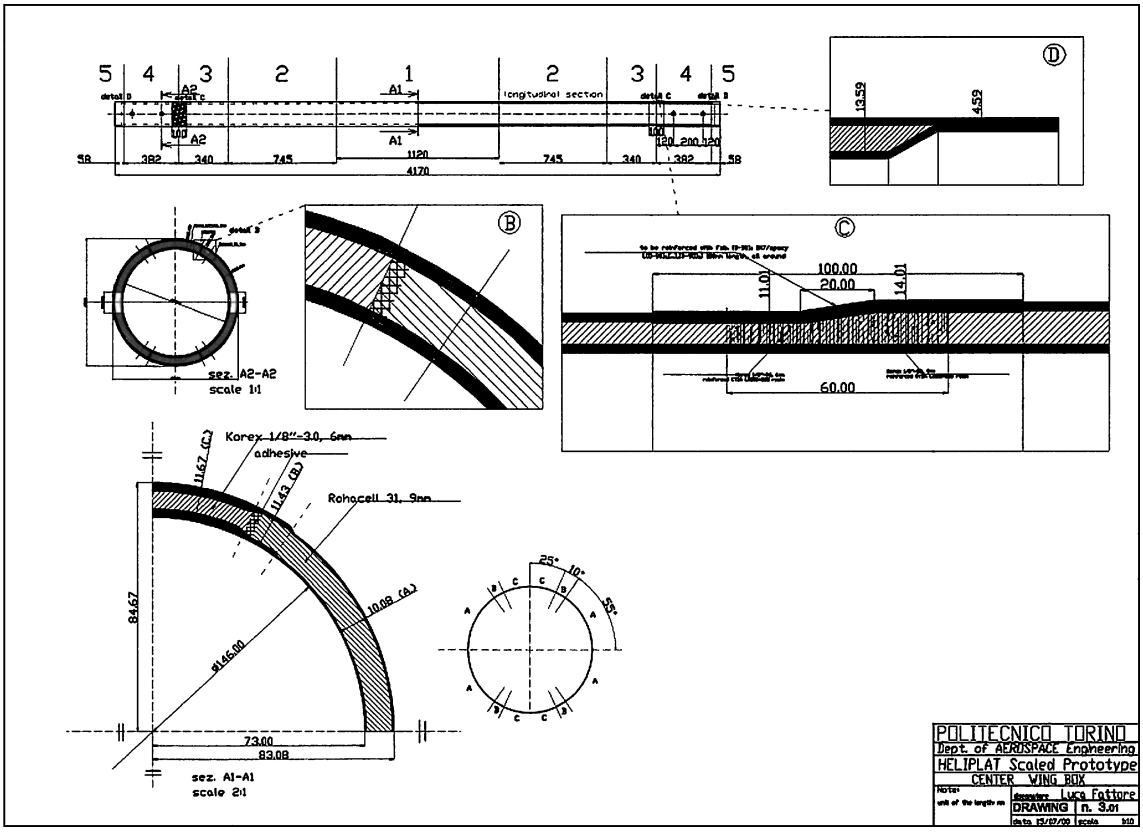

Fig. 18 HeliPlat wing main spar dimensions.

$Re = 5 \times 10^5$, the C_L-α curves are quite similar, and the angular lift coefficient is the same: $C'_L = 5.7$ rad^{-1}. Seeing as the C_D values expected from the numerical data are lower in the considered range than the values obtained from the tests, an increment of up to 10% in the preliminary design was necessitated; the efficiency of the profile was correspondingly reduced in accordance with the test data. The amount of difference between the analytical and experimental C_D can be numerically estimated by considering the different position of the transition point induced by a contamination effect in the flow, particularly in the lower surface of the airfoil. This effect is more pronounced for lower angles of attack because of the particular shape of the profile. A comparison is made with a corresponding pressure distribution both for the case with contamination effects and that without. Furthermore, the effective profile shape is presently being measured to verify correspondence with the theoretical design.

VII. Platform Performance

An accurate aerodynamic analysis of the VESPAA HeliPlat in the final configuration during high-altitude cruise conditions has been carried out by means of the VSAERO CFD code together with the POLITO aerodynamic tool set up.

The twisted wing planform version (PIANTA 8) was employed: the vertical tail has a root chord of 2 m and a tip chord of 1.2 m; the sweep is 35 deg, and the airfoil used is the Fx 71-1-150/20.

The horizontal tail was placed at a height of 3 m from the longitudinal axis of the aircraft; a modified version of the Eppler 228 airfoil was obtained for the tail, by means of the Xfoil code, changing some geometrical parameters (thickness, camber, etc.) to the Eppler 228 airfoil.

The three-dimensional CAD CATIA code was then used to build the body geometry model for the VSAERO code,[19] generating after on the grid with the Pre-processor Spin-g code (Fig. 11). The configuration was completed by adding the fuselage and the boom intersection. The fuselage is a lifting body 3 m wide, 1 m high, and 6.5 m long obtained from a symmetrical profile; the wing–fuselage

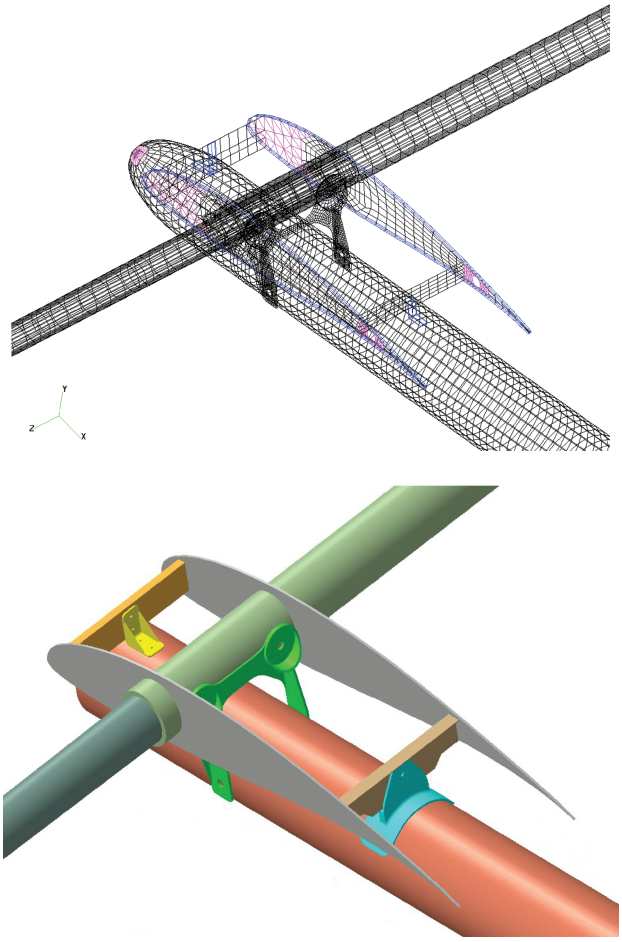

Fig. 19 HeliPlat fittings between wing and boom.

intersection is a medium-height fuse intersection; the boom is 0.6 m wide and passes below the wing. A semi-elliptical shape has been added to the lower part of it to contain the fuel cells and electrolysers system. Finally, the vertical and horizontal tails were added to complete the grid geometry.

The lift coefficient and drag coefficient vs incidence angle, plus the polar of the complete platform, are plotted in Fig. 12. The local C_L of the profiles along the wing at an angle of attack of 5 deg are plotted in Fig. 13; the whole wing lift coefficient is $C_{\text{Ltot}} = 1.354$. In this case the "lifting hole" through the fuselage is less important than at 0-deg angle of attack.

The main factor responsible for total platform drag (pressure drag plus induced drag) is the wing and in particular the outer part. Wing-induced drag corresponds to about 65% of the total drag, whereas wing viscous drag accounts for 30%. In spite of the high aspect ratio of VESPAA, a high lift coefficient is also required at high altitudes to increase the endurance parameter $C_L^{3/2}/C_D$ as well as the aerodynamic efficiency.

Now let us examine the main characteristics of HeliPlat propellers: thrust = 23 N; flight speed = 20 m/s; angular speed = 52.35 rad/s; and propeller radius = 1.15 m.

The effects of the propellers on the platform's aerodynamic behavior have been simulated with VSAERO and are shown in Fig. 14; the upper surface pressure distribution is also plotted. The skin-friction coefficient shown as part of a wing-influenced-by-propeller-wake analysis presents an increased friction coefficient as a result of the transition from laminar to turbulent flow.

The effect of the propellers on the wing lift distribution can also be seen in Fig. 15. Taking into account the propeller-wake analysis determines an efficiency reduction of about 7%.

The stability and control derivatives of the new aircraft configurations are also necessary in the design process. Early determination of the static and dynamic behavior of the aircraft through multidisciplinary design should permit significant improvement in configuration weight, cost, and performances. The classical method of determining static stability and control derivatives—by constructing and testing models in wind tunnels—is very expensive and requires a long lead time for the resultant data. Wind-tunnel tests are also limited to the preselected control effectors of the model. To overcome these shortcomings, we have used the VSAERO code to directly calculate the stability and control derivatives. In the formation of these derivatives, the CFD forces and moments are differentiated with respect to the angle of attack, angle of sideslip, and aircraft shape parameters.

A complete database of the main static and dynamic derivatives has been worked out by using the VSAERO code. When possible, the results have also been compared with classical formulas,[22,23] obtaining the same values.

Fig. 20 HeliPlat scaled-size prototype assembling details.

Yaw angular speed effects on the wake shape of the platform are plotted in Fig. 16.

VIII. Scaled-Size Prototype Structural Design

A scaled-size technological demonstrator has been preliminary designed, with the aim of obtaining a structural and technological proof-of-concept aircraft. The final structural project of the full-scale platform will be carried out and built on the basis of the results obtained from these tests. Taking the preliminary HeliPlat configuration, with its oversized horizontal tail span, as a reference point in the design of the scaled prototype, the wing and tail spans have been reduced to $\frac{1}{3}$ of their final HeliPlat dimensions and the chordwise dimensions to about $\frac{1}{2}$, while the thickness and the layout of the different elements are maintained as for the real configuration. The scaled-size prototype's overall architecture and particular sections of the wing, horizontal tail, and booms are plotted in Fig. 17. The HeliPlat applied loads (resultant bending and torsion moments and resultant shear) take into account the effective aerodynamic and mass distributions according to the JAR-23 /FAR-23 airworthiness requirements. For example, in the limit load condition a maximum bending moment of 38.5 kNm and a shear load of 2.1 kN have been induced at the wing-root section, with a maximum strain of about 1000 $\mu\varepsilon$; the stiffness of each structural element (wing box, tail spars, and booms) has been calculated so that it will guarantee the integrity of the structure up to the ultimate loads.

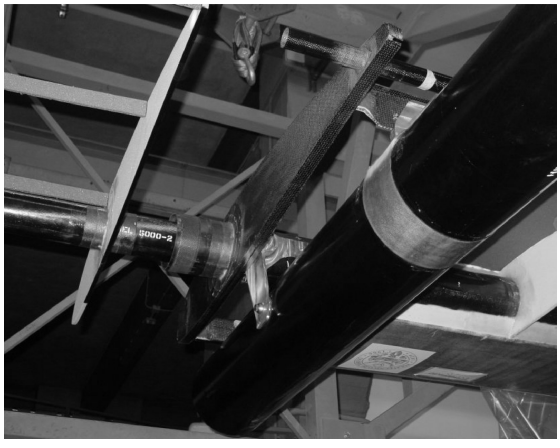

Fig. 21 HeliPlat scaled-size prototype structural details.

A. Wing: Manufacturing and Technological Feasibility

The cross section of the wing is plotted in Fig. 17. The graphite/epoxy main tubular spar will carry all of the shear/ bending/torsion loads applied to the wing, while the leading edge and trailing ribs have (in most cases) a profile shape function and are manufactured in very light rigid foam (Rohacell 51, with a density of 0.051 kg/dm^3) bonded to the spar. The leading edge between the two booms consists of a hand layup glass fiber sandwich panel. The subdivision of the scaled wing structure consists of a 11.2-m-long constant chord inner wing and two 6.57-m-long tapered chord outer wings, one for each side. Two inner-wing elements, each 4.18 m long, connect to a 4.2-m center wing box to make the constant chord wing tubular spar. The inner wing boxes enter the center one for a distance of 0.44 m and are joined with two pairs of bolts (one on the front and one on the rear web). Two 6.57-m-long parts make up the tapered sections, which are connected in a similar way. The main spar is composed of sandwich reinforced tubes made of M55J graphite/epoxy pre-preg tape and Korex or Nomex honeycomb materials. Each tubular spar is autoclave cured at 120°C and 0.3 MPa pressure in a single-cure cycle. The effective and local dimensions and layup of these elements are plotted in Fig. 18.

Some of the ribs are bonded to the tubular spars in the indicated positions, particularly in correspondence to the fittings and engine mounts. A special bolt system has been developed to increase the bearing strength of the composite sandwich fitting.[24] Each pin junction consists of a 28-mm-diam steel-reinforced aperture reaching a final pin hole of 20 mm. The distance between the two front and rear bolts has been calculated so that the design limit load for each bolt is reached. Carbon-fiber-reinforced foam ribs are mounted onto some sections as plotted by "rr" in Fig. 17, while special carbon fiber reinforced plastics (CFRP) honeycomb ribs are mounted in correspondence to the fittings between the several wing spars and above all in correspondence to the booms. All of the ribs are bonded to the spars with a micro-sphere-reinforced glass epoxy.

The CFRP wing boxes were manufactured using M55J graphite/epoxy pre-preg tape. This high-modulus graphite fiber

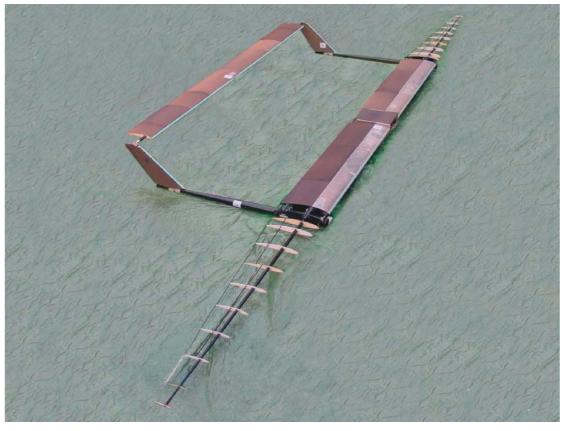

Fig. 22 HeliPlat scaled-size prototype final assembly.

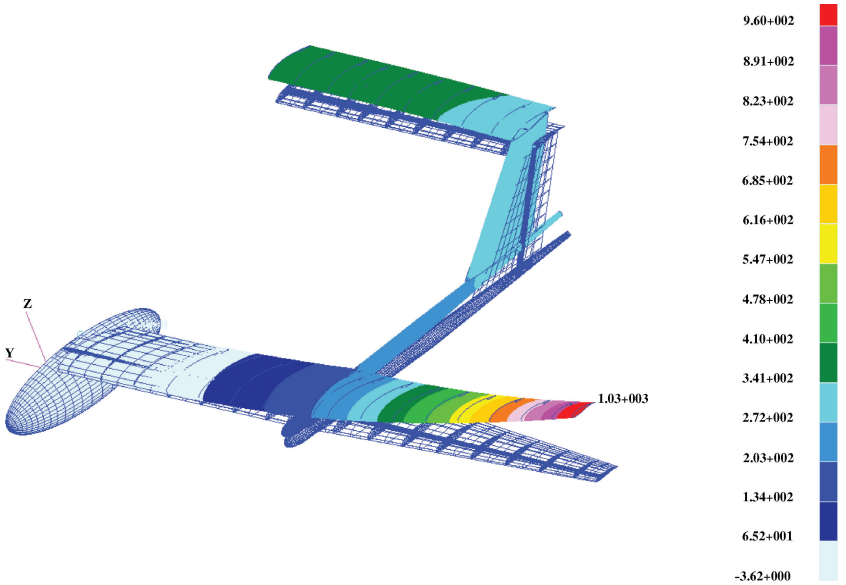

Fig. 23 HeliPlat scaled-size structural configuration, finite element modelization.

greatly increases wing flexural stiffness and reduces the maximum deflection at the wing tip to 1.6 m at the maximum applied limit load.

The laminae used to design the wing boxes have the following main mechanical properties: $E_1 = 279.3$ GPa; $E_2 = 5.84$ GPa; $G_{12} = 4.05$ GPa, $\nu_{12} = 0.36$; $\sigma^t_{1R} = 1036$ MPa; $\sigma^c_{1R} = -381$ MPa; $\varepsilon^t_{1R} = 0.37\%$; and $\rho = 1.58$ kg/dm^3.

The layup of each portion of the single tube was chosen by introducing the just-mentioned mechanical properties into the structural design computer program and can be seen in the corresponding drawing.

B. Horizontal and Vertical Tail: Manufacturing and Technological Feasibility

The scaled horizontal tail structure consists of a constant chord element 11.2 m long (Fig. 17). It is manufactured in three pieces: the inner part of 4.0 m in length and two outer parts, each 3.9 m long. The cross section consists of a main CFRP sandwich tubular spar that will carry all of the shear/bending/torsion loads applied to the horizontal tail. A secondary CFRP rear spar is positioned aft of the main one so as to have a suitable structural support for the elevator systems. The leading and trailing ribs are manufactured in very light rigid foam and are bonded to the box.

The scaled double vertical tail structure consists of a 1.685-m-long tubular spar for each tail, with a circular cross section of 88 mm external diameter. The two spars are made of CFRP sandwich construction, using M55J graphite/epoxy pre-preg tape and Nomex honeycomb.

C. Boom: Manufacturing and Technological Feasibility

The scaled boom-structure consists of a 5.98-m-long tapered tubular member, with a circular 235-mm-diam cross section near the wing box and a 150 mm diam at the vertical tail junction. The 235 mm diam continues up to 2.55 m from the wing box. The two booms are made of CFRP sandwich construction, using M55J graphite/epoxy pre-preg tape and Nomex honeycomb. A special connection based on the introduction of a structural rib has been designed to join the boom to the wing box. The junction (Fig. 19) is composed of three elements: the first (in correspondence to the wing box spar) is a specifically shaped plate; the second (positioned at 0.7 m aft of the wing box spar) consists of a pin-bolted connection; and the third is positioned in correspondence to the rear spar.

D. Scaled-Size Prototype Assembly

CASA Espacio Spain—EADS realized the single CFRP elements of the complete structure (wing, horizontal, and vertical tail tubular spars and reinforced ribs, booms), plus the metal fittings by machine manufacturing.* Because CASA Espacio—EADS decided not to build the entire technological demonstrator, as planned in the European Commission contract, the Department of Aerospace Engineering of the Turin Polytechnic University (Politecnico di Torino) took charge of assembling the various structural components (wing, horizontal and vertical tails, booms), as well as the entire aircraft.

Assemblage was performed by the Italian company ARCHEMIDE Advanced Composites, under the supervision and with the collaboration of the platform design and testing group of the Polytechnic. After all of the different parts were positioned in the proper places so as to define the bonding tree for the junction, they were bonded to the main wing spar (Fig. 20). A rear tubular spar was manufactured by ARCHEMIDE to complete the wing and tail structures.

A reinforced leading edge was designed and manufactured for the center part of the wing to increase torsional stiffness (Fig. 20). The lifting surface was then completed through the positioning of a covering skin. Finally, the assembly was assessed by means of several tests under different conditions. To apply the load during the test activity, the two central ribs were reinforced with a specific dummy structure. Specific metal reinforcements were designed in order to join the different tubular spars, to allow easy assembly and deployment of the prototype and to deal with the problem of bearing in CFRP.[24] A typical joint system is reported in Fig. 20.

Details of the assembled structure are shown in Fig. 21: the main wing-boom joint and the wing. The final structure is represented in Fig. 22, positioned into the steel supporting system for static test activity.

E. Finite Element Method Analysis and Comparison with Experimental Results

A finite element numerical analysis has also been carried out (using the MSC/PATRAN/NASTRAN code) to predict the static and dynamic behavior of the entire structure (Fig. 23). The static finite element method model is composed of 70,000 elements. QUAD4 elements were used to model the CFRP spar laminates, solid HEX8 elements to model the adhesive tape, and the steel bush bonded to the CFRP. (To verify the maximum shear stresses in the adhesive tape, it should be less than 10 MPa.) Because spar laminates present a step tapering along the span, a special mesh procedure is carried out to avoid an element between the tapered thicknesses. The aerodynamic loads are then applied to the several surfaces in equilibrium with the inertia loads. (The highest loads arise on the wing because of the effect of the horizontal tail maneuvering at

*Data available online at http://www.helinet.polito.it/proceedings.asp.

design dive speed.) The first bending mode of the whole scaled-size aircraft has also been calculated, the lowest eigenvalue frequency being 2.2 Hz.

A static test has been carried out on the whole scaled-size prototype. A static test on the complete model seems to be more meaningful than several tests on each element of the structure because several interaction effects can arise when the different elements are tested while assembled:

1) Booms are simultaneously subjected to loads applied by the wing as well as by the horizontal and vertical tails. It would be very difficult to isolate the former without introducing some simplifications, which do not represent the proper boundary conditions.

2) The highest applied loads on the wing derive from the horizontal tail during a pull-up maneuver.

3) The behavior of the horizontal tail is strongly influenced by the constraints to the vertical tail.

To perform a shear-bending-torsion test on the complete scaled-size prototype and verify the theoretical behavior, mechanical equipment was designed and manufactured. A steel supporting structure was defined and manufactured by POLITO in order to sustain the scaled prototype, the tree-beam systems and the hydraulic jack (Fig. 24). The purpose of the tree-beam systems is to reach the defined loading conditions during tests. They are connected by means of steel chains, thereby avoiding spurious loads in the test. Two trolleys support the tree-beam system in such a way that the system adapts to the prototype's deflection behavior. A dummy fuselage was designed for the application of the expected loads at the center of the model.

To date the maximum load applied during the static tests has been 80% of the limit load, corresponding to $n = 2.5$; the test will be carried out up to the ultimate load ($n = 4.5$) to obtain the structural safety margin, after the execution of a fatigue test.

To estimate deformations and wing deflection, strain gauges and transducers were mounted along the wing's main spar. The strain

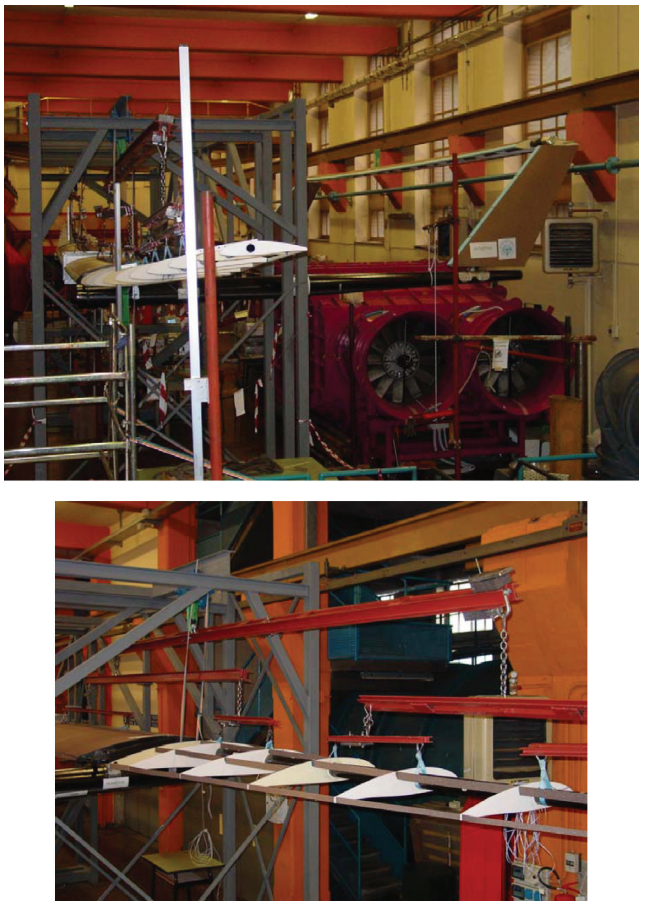

Fig. 24 Mechanical equipment for shear, bending, and torsion test on HeliPlat scaled-size prototype.

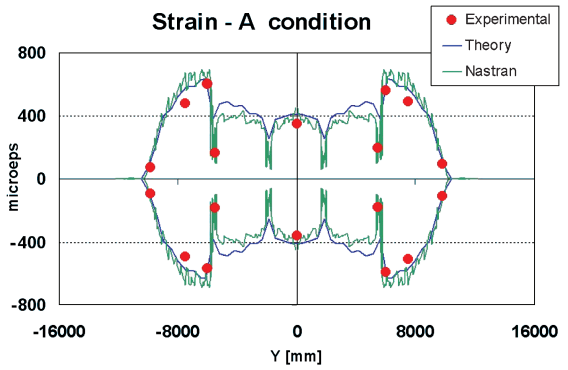

a) Strain results along wing span

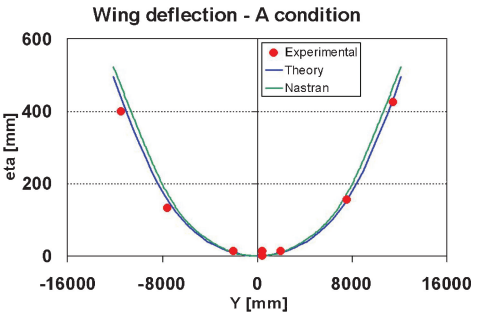

b) Wing deflection along span

Fig. 25 Comparison between analytical and experimental results

results along the wing, for flight conditions corresponding to point A of the n-V diagram, are reported in Fig. 25a; the wing deflection is reported in Fig. 25b; a maximum wing-tip deflection of 400 mm was recorded. A very good correlation has been obtained between analytical, numerical, and experimental results.

IX. Conclusion

The design activity of a new concept platform has been presented including the many different topics involved.

The aerodynamic optimization of the HeliPlat platform (flying at a very high altitude of 17–20 km, a low speed and low Reynolds numbers) has been performed with the computational-fluid-dynamics (CFD) codes VSAERO to increase platform efficiency, in particular to achieve the minimum induced drag vs local Reynolds airfoil (at constant aspect ratio and wing surface).

The numerical airfoil aerodynamic results show that airfoil are capable flying at low Reynolds numbers. The experimental results differ only slightly from the theoretical results, and greater efforts should be made in this field to reduce the gap.

The wing configuration planform has been optimized to reduce platform drag and thus decrease the required flight power.

A platform drag reduction up to 30% has been obtained with respect to the initial platform configuration, giving a reduction in the required flight power and increasing the power available for the payload. A CFD analysis has also been completed, which includes the effect of the eight propellers and has resulted in a 7% increase in the whole drag coefficient. The aerodynamic derivatives have also been obtained in order to evaluate the flight mechanics.

By restricting flight to the spring–autumn months, a smaller platform size could be used and could be manufactured with present-day technologies. The manufacturing of a scaled-size prototype showed the capability of the platform to meet the planned mass and costs.

The finite element method numerical analysis of the scaled-size technological demonstrator shows that the aircraft can meet flexural stiffness requirements. Limited values of wing deflections have in fact been used as design allowables. A good correlation between analytical, numerical, and experimental results has been obtained from the static test on the complete aircraft.

The numerical design of the HeliPlat solar powered platform shows the feasibility of a very long-endurance high-altitude

platform, at least for low-latitude sites in Europe and for six months of operation. A significant reduction in platform size (consequently expanding mission range, altitude, or latitude sites) would occur by increasing solar-cell efficiency to 25%, specific energy of the fuel cells to 600 Wh/kg, and their efficiency to 70%; it is also very important to obtain these performances at a reasonable production cost.

The improvement in the definition of an airfoil database, especially designed for low Reynolds numbers, could increase the platform performances.

It is very important to avoid high structural wing flexibility in order to minimize the aeroelastic effects that could produce undesirable structural failure.

A flight simulation activity is in progress in order to check the specific characteristics obtained during this design process.

Acknowledgments

The authors would like to thank the Italian Space Agency for their financial support: Contracts RS-95-63, ARS-96-136, and ARS-98-167.

The authors would also like to thank the European Commission for the financial support given to the research project HeliNet (network of stratospheric platforms for traffic monitoring, environmental surveillance and broadband services with coordinator Politecnico di Torino) January 2000–April 2003, Fifth Framework Program.

The authors would like to thank A. Porto and M. Fontana for their important contributions to this paper.

References

[1]"Eternal Airplane. The Lift-Off of Unmanned Solar-Electric Wings," *Popular Science*, April 1994, pp. 70–75, 100.

[2]Hall, D. W., Watson, D. A., Tuttle, R. P., and Hall, S. A., "Mission Analysis of Solar Powered Aircraft," NASA CR-172583, July 1985.

[3]Hall, D. W., and Hall, S. A., "Structural Sizing of a Solar Powered Aircraft," NASA CR-172313, April 1984.

[4]Youngblood, J. W., Talay, T. A., and Pegg, R. J., "Design of Long-Endurance Unmanned Airplanes Incorporating Solar and Fuel Cell Propulsion," AIAA Paper 84-1430, June 1984.

[5]Curtin, B., "Solar-Powered UAV Development for NASA," International Technical Conference on "Uninhabited Aerial Vehicles," UAV 2000, EURO-UVS, Paper 10.18, Paris, June 2000.

[6]Romeo, G., "High Altitude Long Endurance Solar Powered Platform for Telecommunication and Earth Observation Applications," Italian Space Agency, Research Contracts RS-95-63, Rome, 1995.

[7]Romeo, G., "Design Proposal of High Altitude Very-Long Endurance Solar Powered Platform for Earth Observation and Telecommunication Applications," International Astronautical Federation, Paper 97-M.2.05, Oct. 1997.

[8]Romeo, G., "Manufacturing and Testing of Graphite-Epoxy Wing Box and Fuselage Structures for a Solarpowered UAV-HAVE," International Council of the Aeronautical Sciences, Paper A98-31591, Sept. 1998.

[9]Romeo, G., "Design of High Altitude Very-Long Endurance Solar Powered Platform for Earth Observation and Telecommunication Applications," *Aerotecnica Missili e Spazio*, Vol. 77, No. 3–4, 1998, pp. 88–99.

[10]Romeo, G., Frulla, G., and Fattore, L., "HELIPLAT: High Altitude Very-Long Endurance Solar Powered UAV for Telecommunication Applications. FEM Analysis, Manufacturing and Testing of 21m long CFRP Wing Box," *Proceedings of the Applied Vehicle Technology Panel Symposium in Unmanned Vehicle for Aerial*, Ground and Naval Military Operations, Ankara, Turkey, NATO, RTO, Neuilly-sur-Seine, France, Oct. 2000, Paper No. 12.

[11]Romeo, G., "Numerical Analysis, Manufacturing and Testing of Advanced Composite Structures for a Solarpowered Airplane," *XV AIDAA National Congress*, Vol. II, AIAA, Rome, 1999, pp. 1001–1012.

[12]Romeo, G., and Frulla, G., "HELIPLAT: Aerodynamic and Structural Analysis of HAVE Solar Powered Platform," *Proceedings of 1st AIAA Technical Conference and Workshop on Unmanned Aerospace Vehicles, Systems, Technologies and Operations*, AIAA, Reston, VA, 2002, Paper No. 3504.

[13]Romeo, G., and Frulla, G., "HELIPLAT®: Design of High Altitude Very-Long Endurance Solar Powered Platform for Telecommunication and Earth Observation Applications," *DASIA Systems in Aerospace*, Paper 9B.4, May 2002.

[14]Profumo, F., Tenconi, A., Gianolio, G., Cerchio, M., Hill-Cottingham, R. J., Coles, P. C., and Eastham, J. F., "A Plastic Structure Multi-DiscAxial Flux PM Motor," *Conference Rec. IEEE-IAS'02*, Vol. 2, pp. 1274–1280.

[15]Prossdorf, S., and Tordella, D., "On an Extension of Prandtl's Lifting Line Theory to Curved Wings," *Impact of Computing in Science and Engineering*, Vol. 3, No. 3, 1991, pp. 191–212.

[16]Frulla, G., "Preliminary Reliability Design of a Solar Powered High Altitude Very Long Endurance Unmanned Air Vehicle," *Journal of Aerospace Engineering*, Paper No. G4, Part G, Vol. 216, 2002, pp. 189–196.

[17]Shooman, M. L., *Probabilistic Reliability : An Engineering Approach*, Krieger, Malabar, FL, 1990.

[18]Drela, M., "XFOIL: An Analysis and Design System for Low Reynolds Number Airfoils," *Low Reynolds Number Aerodynamics*, edited by T. J. Mueller, Lecture Notes in Engineering, Vol. 54, Springer-Verlag, New York, 1989, pp. 1–12.

[19]Nathman, J. K., "VSAERO, A Code for Calculating the Nonlinear Aerodynamic Characteristic of Arbitrary Configuration," User's Manual, Ver. 6.2. Analytical Methods, Inc., Washington, D.C., 2001.

[20]Althauss, D., and Wortmann, F. X., *Stuttgarter Profilkatalog*, 1st ed., Vieweg, Brunswick, Germany, 1981.

[21]Althaus, D., *Niedrig-Geschwindigkeits-Profile*, 1st ed., Vieweg, Brunswick, Germany, 1996.

[22]Etkin, B., *Dynamics of Atmospheric Flight*, 1st ed., Wiley, New York, 1972.

[23]Perkins, C. D., and Hage, R. E., *Airplane Performance Stability and Control*, 1st ed., Wiley, New York, 1960.

[24]Romeo, G., and Frulla, G., "Bearing Strength of Bolted Joints in CFRP Wing Fittings," *International Council of the Aeronautical Sciences*, Paper 396, Sept. 2002.